High-temperature shot noise in the single-channel Aharonov–Bohm interferometer

© R.A. Niyazov[1,2], I.V. Krainov[1], D.N. Aristov[1,2,3], V.Y. Kachorovskii[1]

[1] Ioffe Institute,
194021 St. Petersburg, Russia
[2] Petersburg Nuclear Physics Institute named by B.P. Konstantinov of NRC „Kurchatov Institute“,
188300 Gatchina, Russia
[3] Department of Physics, St. Petersburg State University,
199034 St. Petersburg, Russia

E-mail: niyazov_ra@pnpi.nrcki.ru

Received October 15, 2025
Revised October 29, 2025
Accepted October 29, 2025

Shot noise is theoretically investigated in Aharonov–Bohm interferometers formed by single-channel spinless quantum wires. Analysis focuses on the experimentally important regime of relatively high temperatures, where thermal energy exceeds the level spacing. It is shown that quantum interference effects dramatically alter current fluctuations even when coherence suppression might be expected. The Fano factor — the ratio of shot noise power to Schottky noise — is demonstrated to exhibit sharp, periodically repeating resonances as a function of magnetic flux. For symmetric interferometers, these resonances occur at half-integer flux quanta, while geometric asymmetry leads to additional features at integer flux values. It is found that interferometers with different contact configurations can possess identical conductance but substantially different noise characteristics, enabling experimental determination of contact properties through combined measurements of conductance and noise. The obtained results allow for direct experimental verification and propose noise spectroscopy and characterization of mesoscopic devices as a powerful tool complementary to conductance measurements.

Keywords: Aharonov–Bohm effect, Shot noise, Mesoscopic physics, Quantum interferometry, Fano factor.

DOI: 10.61011/SC.2025.08.62601.8623

1. Introduction

Quantum interferometry represents a cornerstone of mesoscopic physics with profound implications for both fundamental science and technological applications. Among the most striking manifestations of quantum coherence is the Aharonov–Bohm (AB) effect [1,2], where the electron wave function phase becomes sensitive to magnetic flux even in regions free of magnetic fields. This effect forms the basis for high-precision magnetometry and has potential applications in quantum information processing.

The simplest system demonstrating AB oscillations is single-channel interferometer (SCI), i. e. a ring-shaped interferometer with two single-channel arms subjected to perpendicular magnetic field (see Figure 1). Due to the interference of electron trajectories winding around such a setup, the observables, like transmission coefficient and the noise intensity, show Aharonov–Bohm oscillations with a certain periods $\Delta\phi$ as a function of dimensionless magnetic flux $\phi = \Phi/\Phi_0$ threading the device, where $\Phi_0 = hc/e$ is the flux quantum and $\Phi = BS$, where B is homogeneous magnetic field and S is the area of the region encompassed by one-dimensional channel.

At weak tunnel coupling and at low temperatures, the conductance $G(\phi)$ exhibits sharp resonances at certain values of magnetic flux, arising when quantum levels of the system are crossed by the Fermi level [3,4]. As was understood later [5], the case of relatively high temperatures, T, is much less trivial. One might suggest that interference is suppressed when T becomes larger than the level spacing, Δ. However, as was first predicted in Ref. [5] for SCI, the conductance shows interesting interference-induced behavior in this case. Specifically, as it was shown theoretically [5–10] the interference effects lead to resonance behavior of the conductance G even in the case

$$T \gg \Delta = 2\pi v_{\mathrm{F}}/L, \tag{1}$$

where $L = L_1 + L_2$, with $L_{1,2}$ the lengths of the interferometer arms, and v_{F} is the Fermi velocity. However, instead of resonances, $G(\phi)$ exhibits narrow antiresonances under the condition (1). Physically, anti-resonances arise due to trajectories that interfere destructively at any energy ε and, accordingly, are insensitive to energy averaging [6].

The conductance in SCI in the temperature range (1) has been studied in detail, in particular, considering the effects of the electron-electron interaction [6], disorder [8], and spin-orbit interaction [7]. See also discussion for other types of interferometers [11–14].

In this work, we provide a detailed theoretical investigation of the shot noise in SCI. The shot noise is a consequence of the discreteness of the electron charge. We demonstrate that interference effects dramatically modify the Fano factor — the ratio of shot noise power to the Schottky noise value — even when temperature significantly exceeds the level spacing. While conductance oscillations in

such systems have been extensively studied, the shot noise characteristics remain less explored, particularly in the high-temperature regime $T \gg \Delta$, where thermal averaging might be expected to suppress interference effects. Previous works have primarily focused on low-temperature behavior (see review [15]), leaving the interesting regime of thermally robust interference effects largely unexplored. Our analysis reveals that the Fano factor exhibits sharp resonances at specific magnetic flux values, with characteristics highly sensitive to the interferometer geometry and contact properties.

Recently we briefly discussed shot noise in the helical AB interferometer [16], and (for comparision with conventional case) announced without derivation the formula for the Fano factor of the SCI with symmetric arms and identical contacts. In this paper, we provide detailed calculations, and generalize our analysis for the experimentally relevant case of asymmetric arms and non-identical contacts [17–21]. We study in detail the dependence of the noise of a SCI on the magnetic field. Our findings reveal that noise measurements provide complementary information to conductance measurements, allowing determination of contact properties that are indistinguishable through conductance alone.

2. Model

We calculate the current shot noise in spinless single-channel AB interferometer depicted in Figure 1. We model leads by spinless single-channel wires. Although this model of the leads is very simplified, it is commonly used in quantum interferometry, starting from the work [3], since, as we demonstrate below, it allows describing the transition from the metallic leads to the tunnel ones. In particular, this model qualitatively describes quantum point contacts to the interferometer.

The unitarity of scattering matrix of the contact results in backscattering on the contacts [6]. Here, we use this scattering matrix with real-valued elements:

$$\hat{S} = \begin{pmatrix} t_r & t_{\text{out}} & t_{\text{out}} \\ t_{\text{in}} & t_b & t \\ t_{\text{in}} & t & t_b \end{pmatrix},$$

$$t = \frac{1}{1+\gamma}, \quad t_b = -\frac{\gamma}{1+\gamma},$$

$$t_{\text{in}} = t_{\text{out}} = \frac{\sqrt{2\gamma}}{1+\gamma}, \quad t_r = -\frac{1-\gamma}{1+\gamma}. \tag{2}$$

More general case of $\hat{S}$ is discussed in Refs. [22] and [23]. The scattering amplitudes entering Eq. (2) obey $2t_{\text{in}}^2 + t_{\text{r}}^2 = t^2 + t_{\text{b}}^2 + t_{\text{out}}^2 = 1$. The meaning of these amplitudes is illustrated in Figure 2: t_{in} is the amplitude to enter the interferometer into one of the counter-propagating channels, t_{out} is the amplitude to exit the interferometer, t and t_{b} are respectively the amplitudes of forward and backward scattering on the contact inside the interferometer, and t_{r} is the amplitude of backward scattering for electrons coming from the lead. All scattering amplitudes are parameterized by a single parameter $\gamma \in (0, \infty)$.

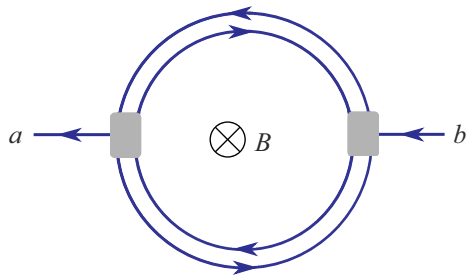

Figure 1. Aharonov–Bohm interferometers based on spinless single-channel quantum wire. The leads (shown by gray color) are also modeled by single-channel spinless wires. Gray regions represent contacts described by 3×3 a S-matrix [see Eqs. (2) and Figures 2]. Homogeneous magnetic field, B, is perpendicular to the picture plane. Corresponding magnetic flux, $\Phi = BS$, is proportional to the area, S, of the region encompassed by one-dimensional channels.

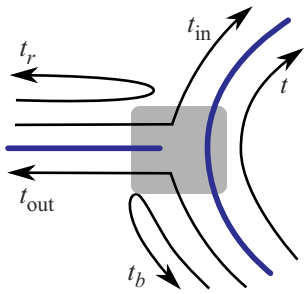

Figure 2. Scattering amplitudes entering scattering matrix Eq. (2) for SCI. The lead is modeled by spinless 1D wire. For tunneling contact, $|t_{\text{r}}| \approx 1$, while the case of metallic contact corresponds to $t_{\text{r}} \to 0$. Contact region with area S_0 is shown by gray color. We assume that $BS_0 \ll \Phi_0$, so that the magnetic field does not affect S-matrix.

The meaning of the parameter γ is further illustrated in Figure 3, see also discussion in Refs. [6,23,24]. The case $\gamma \ll 1$ corresponds to tunneling contact, where almost closed interferometer is weakly coupled to the leads, with γ being a tunneling transparency (see Figure 3, *a*). Interestingly, the case $\gamma \to \infty$ also corresponds to weak tunneling coupling. However, this case is strongly different from the case $\gamma \to 0$, as illustrated in Figure 3 *b*. Metallic contact is modeled by $\gamma \approx 1$ (see Figure 3, *c*). The scattering matrices describing these three cases are given by (see Eq. (2)):

$$\hat{S}(\gamma = 0) = \begin{pmatrix} -1 & 0 & 0 \\ 0 & 0 & 1 \\ 0 & 1 & 0 \end{pmatrix}, \quad \hat{S}(\gamma = \infty) = \begin{pmatrix} 1 & 0 & 0 \\ 0 & -1 & 0 \\ 0 & 0 & -1 \end{pmatrix},$$

$$\hat{S}(\gamma = 1) = \begin{pmatrix} 0 & \sqrt{2} & \sqrt{2} \\ \sqrt{2} & -1 & 1 \\ \sqrt{2} & 1 & -1 \end{pmatrix} /2. \tag{3}$$

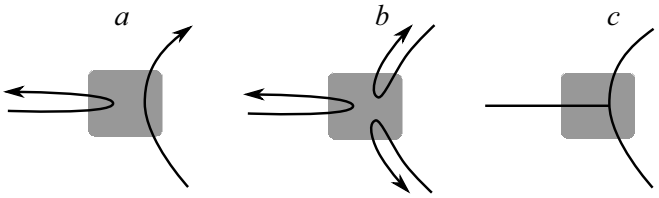

Figure 3. Schematic illustration of different types of leads (contact area is shown by gray color): panels (a) and (b) shows two different types of tunneling coupling, corresponding to $\gamma = 0$ and $\gamma = \infty$, respectively; panel (c) illustrates „metallic" contact, $\gamma \approx 1$. Arrows in panels (a) and (b) show processes with non-zero amplitudes (compare with Figure 2). Panel (c) corresponds to a „metallic contact", so that all processes in Figure 2 are allowed. Scattering matrices, describing cases (a), (b), and (c) are given by Eq. (3).

It is worth noting that $t_b \neq 0$ for any non-zero γ. Below we show that two configurations, Figure 3, a and Figure 3, b, may correspond to the same conductance but to different noise.

3. Shot noise and conductance

3.1. General equations

In this Section, we calculate the Fano factor, $\mathscr{F}$, for setup shown in Figure 1 assuming that a fixed bias voltage V is applied to leads. (In this paper, we assume that the external impedance is zero and therefore the voltage does not fluctuate. For a finite impedance both current and voltage fluctuate as discussed in detail in Ref. [25].)

We will consider the most interesting and easily realized case:

$$\Delta \ll T \ll eV. \tag{4}$$

The current noise is related with fluctuations of the electric current with respect to its average value $\delta\hat{I}(t) = \hat{I}(t) - \langle\hat{I}\rangle$. Here $\hat{I}$ is the current operator (an analytical expression for $\hat{I}$ is given in [25,26]).

The current correlation function associated with the noise is defined by:

$$\mathcal{S}(t-t') = \frac{1}{2}\langle\delta\hat{I}(t)\delta\hat{I}(t') + \delta\hat{I}(t')\delta\hat{I}(t)\rangle\,.$$

The Fourier transform of $\mathcal{S}$ gives an expression for the noise power: $S(\omega) = 2\int_{-\infty}^{\infty} dt\, e^{i\omega t} S(t)$ (the factor 2 in this expression is a matter of convention, see Eq. (1) in Ref. [26] and the comment after Eq. (49) in Ref. [25]).

Transport through the spinless two-terminal device is fully characterized by the transmission energy-dependent amplitude $t(\varepsilon)$ [25,26]:

$$\mathcal{S}(\omega=0) = 2G_0 \int_{\mu}^{\mu+\mathrm{eV}} d\varepsilon\, \mathscr{T}(\varepsilon)\,(1-\mathscr{T}(\varepsilon))\,, \tag{5}$$

where $G_0 = e^2/h$ is the conductance quantum and

$$\mathscr{T}(\varepsilon) = t(\varepsilon)\,t^*(\varepsilon). \tag{6}$$

The averaged current, $I = \langle\hat{I}\rangle$, and the Fano factor are given by

$$eI = G_0 \int_{\mu}^{\mu+\mathrm{eV}} d\varepsilon\, \mathscr{T}(\varepsilon)\,, \tag{7}$$

$$\mathscr{F} = \frac{\mathcal{S}(\omega=0)}{2eI} = \frac{\int_{\mu}^{\mu+\mathrm{eV}} d\varepsilon\, \mathscr{T}(1-\mathscr{T})}{\int_{\mu}^{\mu+\mathrm{eV}} d\varepsilon\, \mathscr{T}}\,. \tag{8}$$

The transmission amplitudes $t_{\alpha\beta}(\varepsilon)$ varies on an energy scale on the order of the level spacing. We focus on the case, when the conditions (4) are satisfied. Then for the $\mathscr{F}$ we have

$$\mathscr{F} = \frac{\langle\mathscr{T}(1-\mathscr{T})\rangle_\varepsilon}{\langle\mathscr{T}\rangle_\varepsilon}, \tag{9}$$

where the averaging is taken over a temperature window in the vicinity of the Fermi level in the limit $T \gg \Delta$. In what follows we assume the linearized form of the spectrum, with $\varepsilon = v_{\mathrm{F}}k$, so that the energy averaging is reduced to calculation of the integral $\langle\cdots\rangle_\varepsilon = \Delta^{-1}\int_0^\Delta d\varepsilon\,(\cdots) = \frac{L}{2\pi}\int_0^{2\pi/L} dk\,(\cdots)$.

As seen from (7), the conductance is proportional to the transmission coefficient averaged over the energy:

$$\mathscr{T} = \langle\mathscr{T}\rangle_\varepsilon \tag{10}$$

Introducing also the average

$$\mathscr{T}_2 = \langle\mathscr{T}\mathscr{T}\rangle_\varepsilon, \tag{11}$$

one can write the Fano factor in the following form:

$$\mathscr{F} = 1 - \frac{\mathscr{T}_2}{\mathscr{T}}. \tag{12}$$

In the next subsection we will discuss calculation that allow one to find $\mathscr{F}$, using Eq. (12). Technically, the key idea is to present the transmission amplitude in a special form, which allows performing the energy averaging analytically.

3.2. Method of calculation

We assume that SCI consists of two arms with the lengths $L/2 \pm a$ and two contacts (not necessarily identical) described by scattering matrices with real amplitudes (see Eq. (2)). We first find convenient expression of transmission amplitude, substitute it into the formula (9), and average over the energy.

We use the method developed in Ref. [8] to sum amplitudes with different winding numbers. We classify all amplitudes of electrons going out of the ring by their direction, either clockwise, $(+)$, or anticlockwise, $(-)$.

For SCI with identical contacts, the amplitudes describing processes of passing the ring in opposite directions without extra revolutions are given by

$$\beta_0 = \begin{pmatrix} \beta_0^+ \\ \beta_0^- \end{pmatrix} = t_{\text{in}} t_{\text{out}} \begin{pmatrix} e^{i(k-2\pi\phi/L)(L/2+a)} \\ e^{i(k+2\pi\phi/L)(L/2-a)} \end{pmatrix}. \qquad (13)$$

All other trajectories finishing at the right lead can be obtained recursively, multiplying by a matrix describing processes which increase number of revolutions, clockwise or counterclockwise, by unity (for a more detailed discussion, see Ref. [8]):

$$\begin{pmatrix} \beta_{n+1}^+ \\ \beta_{n+1}^- \end{pmatrix} = \hat{A} \begin{pmatrix} \beta_n^+ \\ \beta_n^- \end{pmatrix},$$

$$\hat{A} = e^{ikL} \begin{pmatrix} t^2 e^{-i2\pi\phi} + t_b^2 e^{i2ka} & tt_b(e^{-i2\pi\phi} + e^{i2ka}) \\ tt_b(e^{i2\pi\phi} + e^{-i2ka}) & t^2 e^{i2\pi\phi} + t_b^2 e^{-i2ka} \end{pmatrix}. \qquad (14)$$

The full transmission amplitude across the ring is given by:

$$t(\varepsilon) = \sum_{n=0}^{\infty} \alpha \hat{A}^n \beta_0 = \alpha(1-\hat{A})^{-1}\beta_0, \quad \alpha = \begin{pmatrix} 1 \\ 1 \end{pmatrix}, \qquad (15)$$

where β_0 is given by Eq. (13). Having particular expressions for $t(\varepsilon)$, we get $\mathscr{T}(\varepsilon) = |t(\varepsilon)|^2$ and $\mathscr{T}_2(\varepsilon) = |t(\varepsilon)|^4$. The averaging over ε is reduced to integration over the unit circle in complex plane of $z = e^{ikL}$ and is easily performed by residues, see App. A. Most interesting and physically transparent limiting cases are presented below. In the most general case of interferometer with contacts of different strength, the obtained analytical expressions are rather cumbersome and we present them in the App. B.

3.3. Results (symmetric setup, identical contacts)

For the case of a *symmetric* interferometer with equal arm lengths ($a = 0$) and identical contacts, the energy-averaged transmission coefficient [6] is given by

$$\mathscr{T}(\phi, \gamma) = \frac{2\gamma \cos^2(\pi\phi)}{\gamma^2 + \cos^2(\pi\phi)}. \qquad (16)$$

Using formulas from App. A we find the Fano factor in the form (this equation was presented in Ref. [16] without derivation)

$$\mathscr{F}(\phi, \gamma) = 1 - \frac{\cos^2(\pi\phi)\left[5\gamma^2 + \gamma^4 + (1+\gamma^2)\cos^2(\pi\phi)\right]}{2\left[\gamma^2 + \cos^2(\pi\phi)\right]^2}. \qquad (17)$$

Equation (17) is illustrated in Figure 4, where the dependence of Fano factor on the magnetic flux and on the backscattering on the contact, $|t_b| = \gamma/(1+\gamma)$. For three types of tunneling contacts shown in Figure 3, Eq. (17) simplifies:

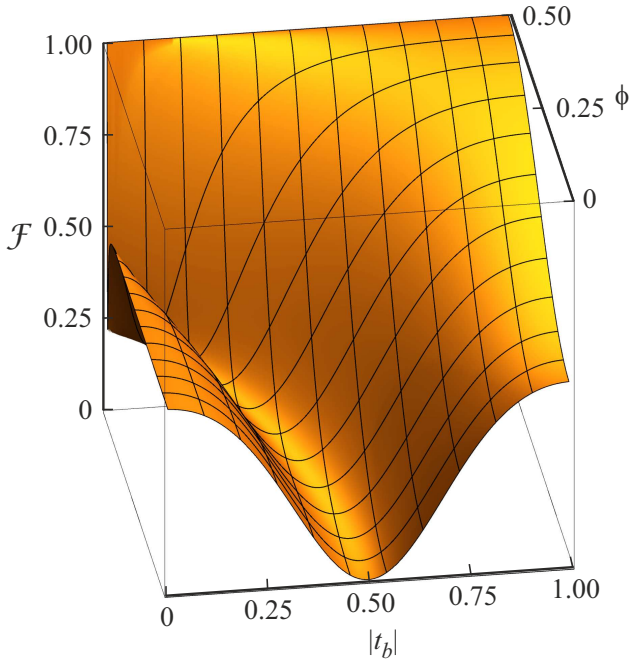

Figure 4. The dependence of Fano factor, $\mathscr{F}(\phi, t_b)$, on the amplitude of backscattering on the contact, t_b, and the magnetic flux, ϕ, as described by Eqs. (2), (16), (17).

$$\mathscr{F}(\phi, 0) = \frac{1}{2},$$

$$\mathscr{F}(\phi, \infty) = 1 - \frac{1}{2}\cos^2(\pi\phi),$$

$$\mathscr{F}(\phi, 1) = \frac{4\sin^2(\pi\phi)}{(\cos(2\pi\phi) + 3)^2}. \qquad (18)$$

The value $1/2$ for $\gamma \to 0$ is a standard value for the Fano factor of tunneling level. We also note that the „metallic“ contacts with $\gamma = 1$, shows both minimal value $\mathscr{F} = 0$, at $\phi = 0$, and to the maximal value, $\mathscr{F} = 1$, at $\phi \to 1/2$.

The dependencies of $\mathscr{T}$ and $\mathscr{F}$ on the magnetic flux are shown in Figures 5, *a*, 5, *b*. The latter figure yields cross-section of Figure 4 for fixed γ. In Figure 5, *a* we see that in the symmetrical interferometer, $a = 0$, the transmission coefficient and the Fano factor have, respectively, sharp antiresonance and sharp resonance at $\phi = 1/2$ (and, hence, at any half-integer flux value).

Several interesting properties of $\mathscr{F}(\phi, \gamma)$ are to be mentioned here. Firstly,

$$\mathscr{F}(0, \gamma) = \mathscr{F}(0, 1/\gamma) = \frac{1}{2}\left(\frac{1-\gamma^2}{1+\gamma^2}\right)^2, \qquad (19)$$

and also

$$\mathscr{T}(0, \gamma) = \mathscr{T}(0, 1/\gamma) = \frac{2\gamma}{1+\gamma^2}.$$

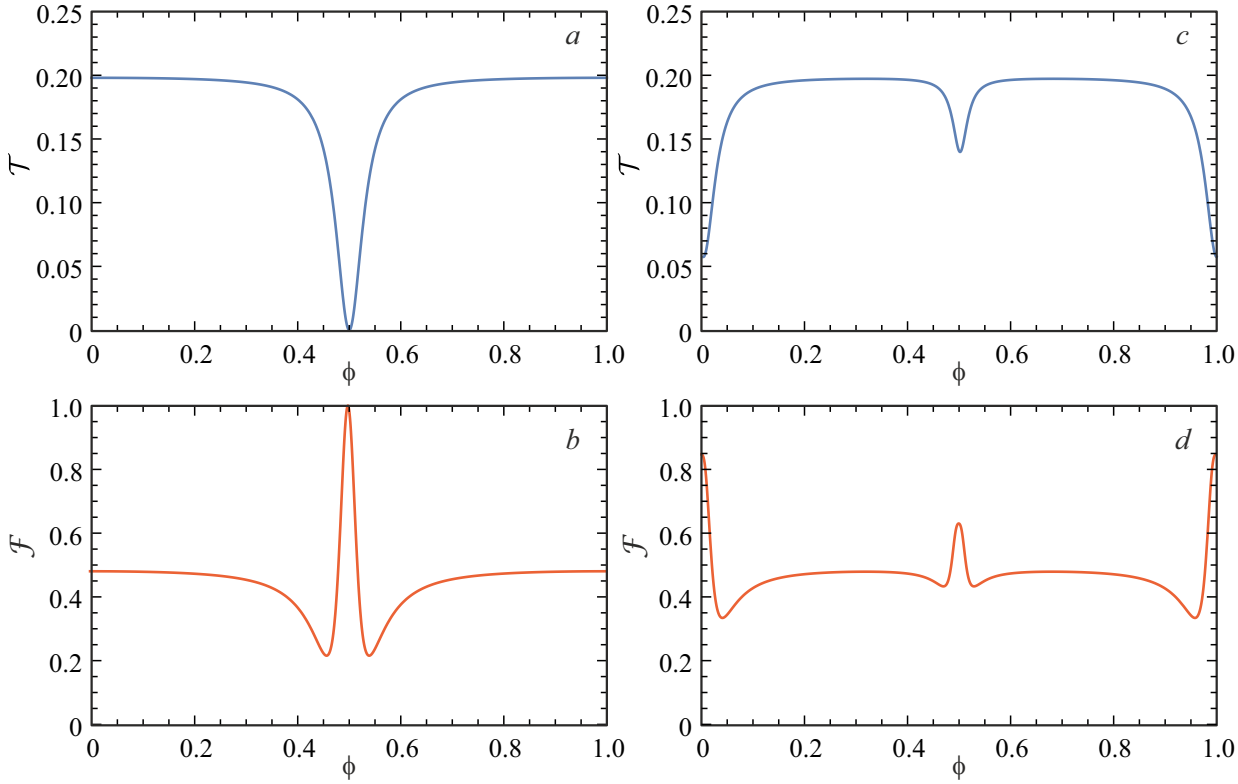

Figure 5. The transmission coefficient (blue curves) and the Fano factor (red curves) for interferometer with two identical contacts. In *symmetric* interferometer with $a = 0$ and weak tunneling coupling ($\gamma = 0.1$) there is antiresonance in $\mathcal{T}$ and resonance in $\mathcal{F}$ at half-integer values of the flux [panels (a) and (b)]. In *asymmetric* interferometer with $a \neq 0$ and weak tunneling coupling ($\gamma = 0.1$, $k_F a = 1.0$), there also appear peaks at integer values of the flux [panels (c) and (d)]. With increasing a, peaks at $\phi = 1/2 + n$ decrease in amplitude and become narrower, while peaks at $\phi = n$ grow and become wider (here, n is integer). Shape of the curve $\mathcal{T}(\phi)$ strongly depends on the asymmetry of the contacts.

It means that for zero flux, the setup with the contacts shown in Figure 3, a with a certain γ is indistinguishable in terms of noise and conductance from the setup with the contacts shown in Figure 3, b with $\gamma_1 = 1/\gamma$.

Let us discuss this point in more detail. As seen from Eq. (19), at $\phi = 0$ the Fano factor and the transmission coefficient are related as follows:

$$\mathcal{F} = \frac{1}{2}\left[1 - \mathcal{T}^2\right]. \tag{20}$$

This equation is shown by red curve in Figure 6 and is valid both for $\gamma < 1$ (i. e. for contacts shown in Figure 3, a) and for $\gamma > 1$ (i. e. for contacts shown in Figure 3, b). Specifically, changing γ from $\gamma = 0$ to $\gamma = \infty$, we pass the red curve twice: once in the interval $0 < \gamma < 1$ and once again for $1 < \gamma < \infty$. This is clearly seen from the cross-section of Figure 4 at $\phi = 0$. We also express Fano factor at $\phi = 0$ (i. e. on the red curve Figure 6, a), via $|t_b|$. Directly from Eq. (19) we find:

$$\mathcal{F}_{\phi=0} = \frac{1}{2}\frac{(|t_b| - 1/2)^2}{[(|t_b| - 1/2)^2 + 1/4]^2}.$$

Importantly, the Fano factor has minimum with zero minimal value in the „metallic“ point, $t_b = 1/2$ ($\gamma = 1$). This property is lost in presence of magnetic flux, see Figure 4.

For $\phi \neq 0$, the red curve splits into two curves, as shown in Figure 6 by blue, green and orange lines. Notice that the Fano factor can have two values for the same value of the transmission coefficient, corresponding to two different γ. Remarkably, there is a special singular point, $\phi = 1/2$, where the conductance is exactly zero (see [3] and a more detailed discussion of this property in [6]). At this point, the Fano factor becomes unity for fixed γ:

$$\mathcal{T}(1/2, \gamma) = 0, \quad \mathcal{F}(1/2, \gamma) = 1. \tag{21}$$

The behavior of the Fano factor near this point is illustrated by the orange curve in Figure 6, a, which corresponds to $\phi = 0.48$. The transmission coefficient and the Fano factor for $|\delta\phi| = |\phi - 1/2| \ll 1$, weak tunneling coupling, $\gamma \ll 1$, and arbitrary ratio

$$x = \pi\delta\phi/\gamma.$$

are given by the following expressions

$$\mathcal{T}(\delta\phi, \gamma) \approx 2\gamma\,\frac{x^2}{1 + x^2}, \tag{22}$$

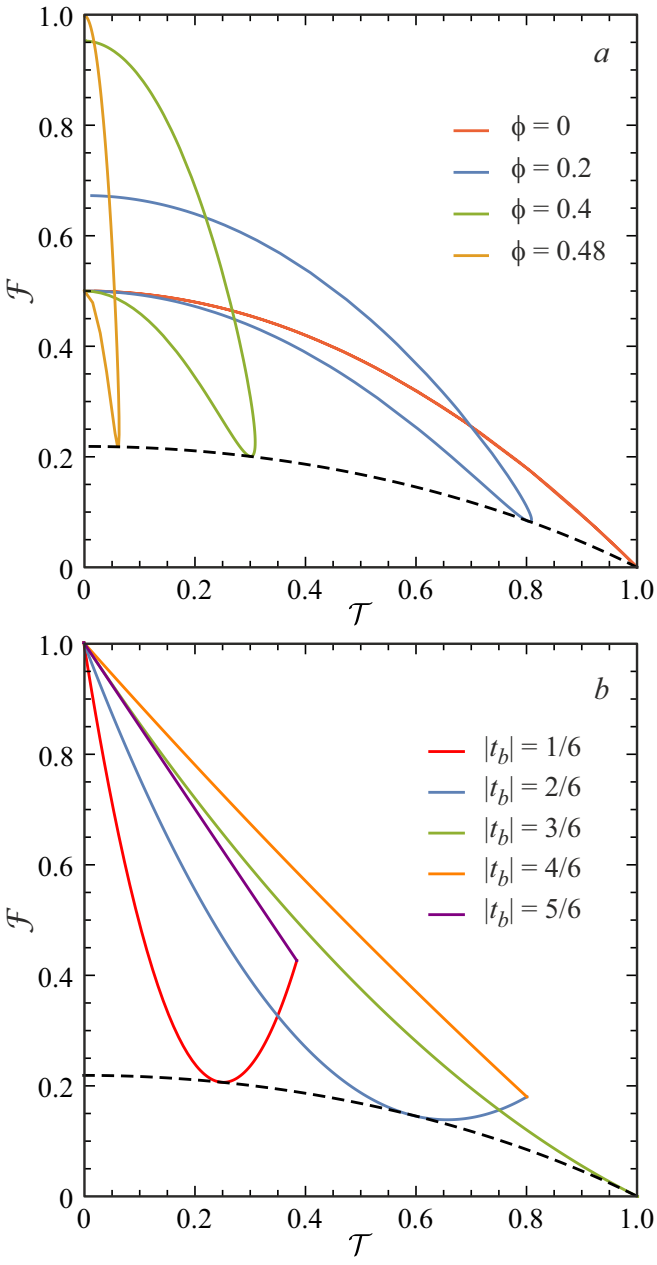

Figure 6. Parametric plot $(\mathscr{T}, \mathscr{F})$ for fixed ϕ and $0 < \gamma < \infty$ (a), for fixed $|t_b| = \gamma/(1+\gamma)$ and $0 < \phi < 1$ (b).

$$\mathscr{F}(\delta\phi, \gamma) \approx \frac{2 - x^2 + x^4}{2(1+x^2)^2}, \tag{23}$$

Hence, the value of $\mathscr{F}$ depends on the order of taking the limits $\delta\phi \to 0$ and $\gamma \to 0$, so that if we fix $\delta\phi$ and tend γ to zero, then instead of Eq. (21) we get the usual expression for the tunnel contact:

$$\mathscr{F} \to 1/2, \quad \gamma \to 0, \quad \delta\phi \text{ is fixed.}$$

From Eqs.(23) we can get an analytical expression describing the orange line in Figure 6, *a*. To this end, we fix $\delta\phi$ and change tunneling coupling from $\gamma = 0$ to relatively large value: $\delta\phi \ll \gamma \ll 1$. Then, we get at $0 < \mathscr{T} < \pi|\delta\phi|$:

$$\mathscr{F} \approx \frac{3}{4} - \frac{1}{2}\frac{\mathscr{T}}{\pi\delta\phi} \pm \frac{1}{4}\sqrt{1 - \left(\frac{\mathscr{T}}{\pi\delta\phi}\right)^2}. \tag{24}$$

The sign in front of the last term distinguish two branches of the orange curve. The minimum of $\mathscr{F}$ is reached at the lower branch at $\mathscr{T} = 15\pi|\delta\phi|/16$ and is given by $\mathscr{F} = 17/32$, which is the value of the dashed line in Figure 6, *a* for $\mathscr{T} = 0$.

In Figure 6, *a* we fixed ϕ and changed γ from zero to infinity. Fixing γ instead and changing ϕ in the interval $0 < \phi < 1$, we find the following expression connecting transmission coefficient and the Fano factor valid for any γ in the interval $0 < \gamma < \infty$:

$$\mathscr{F} = 1 - \frac{5+\gamma^2}{2}\frac{\mathscr{T}}{2\gamma} + 2\left(\frac{\mathscr{T}}{2\gamma}\right)^2, \tag{25}$$

$$0 < \mathscr{T} < \frac{2\gamma}{1+\gamma^2}.$$

This equation has minimum at $\mathscr{T}_{\min} = (5+\gamma^2)\gamma/4$ given by $\mathscr{F}_{\min} = [7 - \gamma^2(10+\gamma^2)]/32$. The family of the curves described by Eq. (25) for different γ is shown in Figure 6, *b*. Note that the dashed curves in panels (a) and (b) of Figure 6 coincide. From above discussion, we see that behavior of the noise of SCI is very singular for ϕ close to $1/2$. This means that noise is very sensitive to the flux in the vicinity of this point.

3.4. Results (asymmetric setup)

The asymmetry of setup becomes important when $a \geq k_F^{-1}$. For not too large voltages, $eV \ll v_F/a$, one can replace $ka \to k_F a$ in scattering amplitudes. The expression for the transmission coefficient in asymmetric setup was obtained earlier in Ref. [6]. Analytical expression for the Fano factor in this case can be found by using formulas presented in App. A and App. B. Its general form is too cumbersome and we present it here only for the flux values close to integer and half-integer number and for weak tunneling coupling.

For $\delta\phi = |\phi - 1/2| \ll 1$ and $\gamma \ll 1$ the Fano factor reads:

$$\mathscr{F}_{1/2}(\delta\phi, \gamma) = \frac{2 - \bar{x}^2 + \bar{x}^4}{2(1+\bar{x}^2)^2} + \frac{\sin^2(k_F a)[3\bar{x}^2 - \sin^2(k_F a)]}{2(1+\bar{x}^2)[\bar{x}^2 + \sin^2(k_F a)]}, \tag{26}$$

where

$$\bar{x} = \frac{\pi\,\delta\phi}{\gamma\cos(k_F a)}.$$

Similar to Eq. (23), the value of $\mathscr{F}_{1/2}$ at $\delta\phi \to 0$, $\gamma \to 0$ depends on the order of limits. Fixing $\delta\phi$ and decreasing

the tunneling coupling to zero, $\gamma \to 0$, we get $\bar{x} \to \infty$, so that $\mathscr{T}_{1/2} \to 1/2$. Putting $\delta\phi$ to zero first, we find

$$\mathscr{T}_{1/2} \to 1 - \frac{\sin^2(k_F a)}{2}. \tag{27}$$

It turns out, that the Eq. (26) also describes the case of small magnetic flux, $|\phi| \ll 1$, if we set $\delta\phi = \phi$ there and replace $k_F a$ by $k_F a + \pi/2$.

As seen from Eqs. (26) and (27), the asymmetry of the device strongly affect the noise intensity even for fixed magnetic flux, so that changing a within a small interval about the Fermi wavelength, we change $\mathscr{T}$ by a factor on the order of two.

The dependencies of $\mathscr{T}$ and $\mathscr{F}$ on the magnetic flux, ϕ, are shown in Figure 5, *c* and 5, it d. Comparing these figures with Figure 5, *a* and 5, *b* plotted for symmetric case, we see that new peaks at integer values of the flux appear for $a \neq 0$ both in the transmission coefficient (antiresonances) and in the Fano factor (resonances) for integer values of flux. With increasing asymmetry, the amplitudes of the peaks corresponding to half-integer values of the flux decrease, while the amplitudes of the peaks at integer flux values increase. We conclude that asymmetry of the device, which is always present in real experiments [17–21], strongly modifies shot noise.

3.5. Results (different tunneling couplings)

In this subsection, we present results for the case of symmetric setup, $a = 0$, but different right and left contacts, characterized by parameter, γ_R and γ_L, respectively. Using general equations presented in App. B and performing standard energy averaging with the use of formulas from App. A, one can find the following expressions for the transmission coefficient and Fano factor:

$$\mathscr{T}(\phi, \gamma_R, \gamma_L) = \kappa^{-1/2} \frac{2\bar{\gamma}\cos^2(\pi\phi)}{\bar{\gamma}^2 + \cos^2(\pi\phi)},$$

$$\mathscr{F}(\phi, \gamma_R, \gamma_L) = 1 - \kappa^{-1} \frac{\cos^2(\pi\phi)}{2(\bar{\gamma}^2 + \cos^2(\pi\phi))^2} \times \left((1+4\kappa)\bar{\gamma}^2 + \bar{\gamma}^4 + (1+\bar{\gamma}^2)\cos^2(\pi\phi)\right),$$

where

$$\bar{\gamma} = \sqrt{\gamma_L \gamma_R}, \quad \kappa = (\gamma_L + \gamma_R)^2/4\gamma_L\gamma_R.$$

The analog of Eq. (20) at $\phi = 0$ for different right and left contacts attains the form

$$\mathscr{F} = 1 - \frac{1}{2\kappa} - \frac{\kappa}{2}\mathscr{T}^2. \tag{28}$$

4. Conclusion

In this paper, we have presented a comprehensive theoretical analysis of shot noise in spinless single-channel Aharonov–Bohm interferometers, focusing on the experimentally relevant high-temperature regime $T \gg \Delta$. Our key findings demonstrate that quantum interference effects leave distinct signatures in the current noise spectrum, even when thermal averaging might be expected to suppress interference.

We have shown that the Fano factor exhibits characteristic periodic resonances as a function of magnetic flux, with sharp features at both integer and half-integer flux quanta. The exact nature of these resonances depends sensitively on the interferometer geometry: symmetric interferometer display antiresonances in conductance and corresponding resonances in noise at half-integer flux values, while asymmetric geometries develop additional features at integer flux values.

A particularly important result concerns the complementary information provided by simultaneous measurement of conductance and noise. We demonstrated that different contact configurations — specifically the two distinct tunneling contact types corresponding to $\gamma \to 0$ and $\gamma \to \infty$ — can yield identical conductance but markedly different noise characteristics (see, for example, limit $\mathscr{T} \to 0$ in the Figure 6, *a*). This provides a powerful experimental tool for characterizing contact properties in nanoscale devices.

The sensitivity to geometric asymmetry, always present in real fabricated devices [17–21], underscores the importance of our generalized treatment beyond the idealized symmetric case. Our results show that even small asymmetries on the scale of the Fermi wavelength can substantially modify the noise characteristics.

From an experimental perspective, our predictions are testable with existing nanofabrication capabilities. The condition $T \gg \Delta$ corresponds to temperatures above a few Kelvin for micron-scale devices, making these effects accessible in standard cryogenic setups. The predicted sharp features in the flux dependence of the Fano factor provide clear experimental signatures.

In summary, shot noise measurements in single-channel AB interferometers offer a rich probe of quantum coherence effects that survive thermal averaging. The complementary information provided by noise, beyond what can be learned from conductance alone, makes this an valuable diagnostic tool for characterizing mesoscopic devices and their contacts.

Funding

The work was carried out with financial support from the Russian Science Foundation (grant No. 25-12-00212), https://rscf.ru/project/25-12-00212/.

Conflict of interest

The authors of this work declare that they have no conflicts of interest.

A. Energy averaging

Throughout the paper we average observable quantities over a small temperature window in the vicinity of the Fermi level in the limit $T \gg \Delta$. For the linearized form of the spectrum, with $\varepsilon = v_F k$, the energy averaging is reduced at high temperatures to calculating the integral $\langle \cdots \rangle_\varepsilon = \Delta^{-1} \int_0^\Delta d\varepsilon \, (\cdots) = \frac{L}{2\pi} \int_0^{2\pi/L} dk \, (\cdots)$.

The averaging over kL, is reduced to integration over the unit circle $z = e^{ikL}$ in complex plane and is easily performed by residues. The formulas which were used for calculations are listed below:

$$\left\langle \prod_{j=1}^{4} \frac{1}{(1-\tau_j e^{\alpha i k L})^{n_j}} \right\rangle_\varepsilon = 1\,, \quad n_j = 0,\ 1,$$

$$\left\langle \frac{1}{(1-\tau_1 e^{\alpha i k L})} \frac{1}{(1-\tau_2 e^{-\alpha i k L})} \right\rangle_\varepsilon = \frac{1}{1-\tau_1\tau_2}\,,$$

$$\left\langle \frac{1}{(1-\tau_1 e^{\alpha i k L})} \frac{1}{(1-\tau_2 e^{-\alpha i k L})} \frac{1}{(1-\tau_3 e^{-\alpha i k L})} \right\rangle_\varepsilon = \frac{1}{(1-\tau_1\tau_2)(1-\tau_1\tau_3)}\,,$$

$$\left\langle \frac{1}{(1-\tau_1 e^{\alpha i k L})} \frac{1}{(1-\tau_2 e^{-\alpha i k L})} \frac{1}{(1-\tau_3 e^{-\alpha i k L})} \frac{1}{(1-\tau_4 e^{-\alpha i k L})} \right\rangle_\varepsilon = \frac{1}{(1-\tau_1\tau_2)(1-\tau_1\tau_3)(1-\tau_1\tau_4)}\,,$$

$$\left\langle \frac{1}{(1-\tau_1 e^{\alpha i k L})} \frac{1}{(1-\tau_2 e^{\alpha i k L})} \frac{1}{(1-\tau_3 e^{-\alpha i k L})} \frac{1}{(1-\tau_4 e^{-\alpha i k L})} \right\rangle_\varepsilon = \frac{1-\tau_1\tau_2\tau_3\tau_4}{(1-\tau_1\tau_3)(1-\tau_2\tau_3)(1-\tau_1\tau_4)(1-\tau_2\tau_4)}\,, \tag{29}$$

where $\alpha = \pm 1$ and all $|\tau_j| < 1$.

B. Interferometer with non-equal arms and non-identical contacts

In this Appendix, we present generalization of the tunneling amplitude $t(\varepsilon)$ (see Eq. (15)) for the case of non-identical contacts having different tunneling couplings. The symmetric case is obtained by putting $t_{\text{in,L}} = t_{\text{in,R}} = t_{\text{in}}$, etc. in equations presented below.

$$t(\varepsilon) = \sum_{n=0}^{\infty} \vec{\alpha} \hat{A}^n \vec{\beta}_0, \quad \vec{\alpha} = \begin{pmatrix} 1 \\ 1 \end{pmatrix}, \quad \vec{\beta} = \begin{pmatrix} \beta_0^+ \\ \beta_0^- \end{pmatrix} = t_{\text{in},L} t_{\text{out},R} \begin{pmatrix} e^{i(k-2\pi\phi/L)(L/2+a)} \\ e^{i(k+2\pi\phi/L)(L/2-a)} \end{pmatrix},$$

$$\hat{A} = e^{ikL} \begin{pmatrix} t_L t_R e^{-i2\pi\phi} + t_{b,L} t_{b,R} e^{i2ka} & t_L t_{b,R} e^{-i2\pi\phi} + t_{b,L} t_R e^{i2ka} \\ t_L t_{b,R} e^{i2\pi\phi} + t_{b,L} t_R e^{-i2ka} & t_L t_R e^{i2\pi\phi} + t_{b,L} t_{b,R} e^{-i2ka} \end{pmatrix}. \tag{30}$$

After some algebra one can rewrite expression for $t(\varepsilon)$ as follows:

$$t(\varepsilon) = t_{\text{in},L} t_{\text{out},R} e^{-i2\pi\phi a/L} \left(\frac{Z e^{i(kL/2-\pi\phi)}}{1-\tilde{t}^2 e^{ikL-2\pi\phi}} + \frac{Z^*|_{L\leftrightarrow R} e^{i(kL/2+\pi\phi)}}{1-\tilde{t}^{*2} e^{ikL+2\pi\phi}} \right),$$

$$Z = i \frac{Z_1 Z_2}{Z_3} e^{i\pi\phi},$$

$$Z_1 = Z_4 - (t_{b,L} - t_L)(t_{b,R} \sin(2ak) + t_R \sin(2\pi\phi)) - i(t_{b,R} t_L \cos(2ak) + t_{b,L} t_R \cos(2\pi\phi)),$$

$$Z_2 = Z_4 + (t_{b,R} - t_R)(t_{b,L} \sin(2ak) + t_L \sin(2\pi\phi)) - i(t_{b,L} t_R \cos(2ak) + t_{b,R} t_L \cos(2\pi\phi)),$$

$$Z_3 = 2Z_4 \left(t_{b,L} t_R e^{-i(ak+\pi\phi)} + t_{b,R} t_L e^{i(ak+\pi\phi)} \right),$$

$$Z_4^2 = \left(t_{b,L}^2 - t_L^2\right)\left(t_{b,R}^2 - t_R^2\right) - (t_{b,L} t_{b,R} \cos(2ak) + t_L - t_R \cos(2\pi\phi))^2,$$

$$\tilde{t}^2 = iZ_4 + t_{b,L} t_{b,R} \cos(2ak) + t_L t_R \cos(2\pi\phi)\,. \tag{31}$$

Assuming that $eV \ll v_F/a$, one can replace $ka \to k_F a$ in this equation. Now we see that the expressions $|t(\varepsilon)|^2$, $|t(\varepsilon)|^4$ contain the complex quantity e^{ikL} which is regarded as a new variable. Then, one can perform averaging of these expressions over energy by using formulas derived in App. A.

References

[1] Y. Aharonov, D. Bohm. Phys. Rev., **115** (3), 485 (1959).
[2] Y. Aharonov, D. Bohm. Phys. Rev., **130** (4), 1625 (1963).
[3] M. Büttiker, Y. Imry, M.Y. Azbel. Phys. Rev. A, **30** (4), 1982 (1984).
[4] M. Büttiker, Y. Imry, R. Landauer, S. Pinhas. Phys. Rev. B, **31** (10), 6207 (1985).
[5] E.A. Jagla, C.A. Balseiro. Phys. Rev. Lett., **70** (5), 639 (1993).
[6] A.P. Dmitriev, I.V. Gornyi, V.Y. Kachorovskii, D.G. Polyakov. Phys. Rev. Lett., **105** (3), 036402 (2010).
[7] P.M. Shmakov, A.P. Dmitriev, V.Y. Kachorovskii. Phys. Rev. B, **85** (7), 75422 (2012).
[8] P.M. Shmakov, A.P. Dmitriev, V.Y. Kachorovskii. Phys. Rev. B, **87** (23), 235417 (2013).
[9] A.P. Dmitriev, I.V. Gornyi, V.Y. Kachorovskii, D.G. Polyakov, P.M. Shmakov. JETP Lett., **100** (12), 839 (2015).
[10] A.P. Dmitriev, I.V. Gornyi, V.Y. Kachorovskii, D.G. Polyakov. Phys. Rev. B, **96** (11), 115417 (2017).
[11] D.E. Feldman, Y. Gefen, A. Kitaev, K.T. Law, A. Stern. Phys. Rev. B, **76** (8), 085333 (2007).
[12] C. Wang, D.E. Feldman. Phys. Rev. B, **82** (16), 165314 (2010).
[13] G. Yang. Phys. Rev. B, **91** (11), 115109 (2015).
[14] R.A. Niyazov, D.N. Aristov, V.Y. Kachorovskii. npj Comput. Mater., **6** (1) (2020).
[15] K. Kobayashi, M. Hashisaka. J. Phys. Soc. Jpn., **90** (10), 102001 (2021).
[16] R.A. Niyazov, I.V. Krainov, D.N. Aristov, V.Y. Kachorovskii. JETP Lett., **119** (5), 372 (2024).
[17] H.R. Shea, R. Martel, P. Avouris. Phys. Rev. Lett., **84** (19), 4441 (2000).
[18] V. Piazza, F. Beltram, W. Wegscheider, C.-T. Liang, M. Pepper. Phys. Rev. B, **62** (16), R10630 (2000).
[19] A. Fuhrer, S. Lüscher, T. Ihn, T. Heinzel, K. Ensslin, W. Wegscheider, M. Bichler. Nature, **413** (6858), 822 (2001).
[20] U.F. Keyser, C. Fühner, S. Borck, R.J. Haug, M. Bichler, G. Abstreiter, W. Wegscheider. Phys. Rev. Lett., **90** (19), 196601 (2003).
[21] S. Zou, D. Maspoch, Wang, C.A. Mirkin, G.C. Schatz. Nano Lett., **7** (2), 276 (2007).
[22] D.N. Aristov, P. Wölfle. Phys. Rev. B, **84** (15), 155426 (2011).
[23] D.N. Aristov, A.P. Dmitriev, I.V. Gornyi, V.Y. Kachorovskii, D.G. Polyakov, P. Wölfle. Phys. Rev. Lett., **105** (26), 266404 (2010).
[24] D.N. Aristov, I.V. Gornyi, D.G. Polyakov, P. Wölfle. Phys. Rev. B, **95** (15), 155447 (2017).
[25] Y. Blanter, M. Büttiker. Phys. Rep., **336** (1-2), 1 (2000).
[26] M.J.M. de Jong, C.W.J. Beenakker. *Mesoscopic Electron Transport*, L. Sohn, L. Kouwenhoven, G. Schön, 345 *NATO ASI Series E*, 225–258, (Kluwer Academic Publishing, Dordrecht, 1997).